JOURNAL OF MATERIALS SCIENCE 28 (1993) 3221–3227

Plaster of Paris as a model material for brittle porous solids

G. VEKINIS*, M. F. ASHBY, P. W. R. BEAUMONT
Cambridge University Engineering Department, Trumpington Street, Cambridge CB2 1PZ, UK

Plaster of Paris is a brittle, porous solid, easy to shape, which has potential as a model material for the study of brittle, porous, solids such as ceramics, rocks and cement. This paper describes the mechanical properties of plaster of Paris – modulus, strength, fracture toughness, etc. – as a function of porosity. The material is then used to study the initiation and propagation of cracks in compression, as a function of porosity, stress state and stress concentration.

1. Introduction

Plaster of Paris (hydrated calcium sulphate) is a brittle solid with fracture properties which resemble those of cement, sandstone, and other porous ceramics. It can be shaped easily, and used as a model material to study the behaviour, under load, of porous solids containing macroscopic cracks, holes and reinforcement. The first part of this paper reports a study of the properties of plaster of Paris – the modulus, tensile and compressive strengths, modulus of rupture, and fracture toughness – as a function of the density (or porosity) of the plaster.

The second part describes an example of an application: the mechanisms of failure at a cylindrical hole or spherical pore under simple and multiaxial compression. Stress is concentrated at a macroscopic hole in an elastic solid. In uniaxial compression, tension appears at one pair of poles of the pore; but in most biaxial compression states all principal stresses at and near the pore are zero or compressive. Despite this, fracture occurs at the pore surface in a porous or micro-cracked material like plaster, causing inward spalling of material from the pore surface. The problem is known in the mining industry, when geostatic loads cause inward spalling of boreholes, and it is probably the mechanism by which fracture starts in porous ceramics under compressive stress states. We have used plaster of Paris samples to investigate the initiation and progress of cracking from holes and pores, under a variety of stress states. The results are related to observations and models for compressive failure of brittle solids [1–16].

2. Plaster of Paris: the material

Plaster of Paris is calcium sulphate hemihydrate, $CaSO_4 \cdot \frac{1}{2}H_2O$. It is made by heating gypsum between 120 and 160 °C

$$CaSO_4 \cdot 2H_2O \rightleftharpoons CaSO_4 \cdot \tfrac{1}{2}H_2O + 1\tfrac{1}{2}H_2O \quad (1)$$

When plaster of Paris is mixed with water the reverse reaction takes place: water is reabsorbed with the formation of gypsum. The reaction is exothermic and results in a coherent mass of interlocking needle-shaped gypsum crystals. The chemistry of the reaction requires only 18.6 wt % water for rehydration, but in practice much more is used to give the fluidity needed for casting. The excess water evaporates leaving considerable porosity. The true density of the hemihydrate is about 2750 kg m^{-3} and that of the dihydrate about 2320 kg m^{-3}, so a contraction on setting would be expected; but the arrangement of the crystals is such that setting results in a slight expansion (about 0.5%).

The mechanical properties of plaster depend on powder-to-water ratio, curing time, temperature and pressure, and on post-cure heat treatment. All were investigated [16] and a standard procedure was adopted. The $CaSO_4 \cdot \frac{1}{2}H_2O$ starting powder (British Drug House) was mixed with distilled water, in the ratio 100 : 62.5, removing all air trapped in the suspension, and was cast into split rectangular (approximate size 10 mm × 10 mm × 100 mm) or cylindrical (approximate size 10 mm diameter × 80 mm height) moulds and allowed to cure for at least 7 days at 20 °C. Specimens of higher density than that of the as-cast specimens were obtained by forcing water out of the mould under pressure, immediately after casting. The samples contain small spherical pores (Fig. 1), probably due to trapped water during casting, which decrease in size with increasing bulk density of the material (Fig. 2).

3. The mechanical properties of plaster of Paris

3.1. Plain specimens

A number of mechanical properties were measured as a function of density. The properties included Young's

* *Present address*: "Demokritos" National Centre for Scientific Research, Institute of Materials Science, 153 10 Ag Paraskevi Attikis, Athens, Greece.

0022–2461

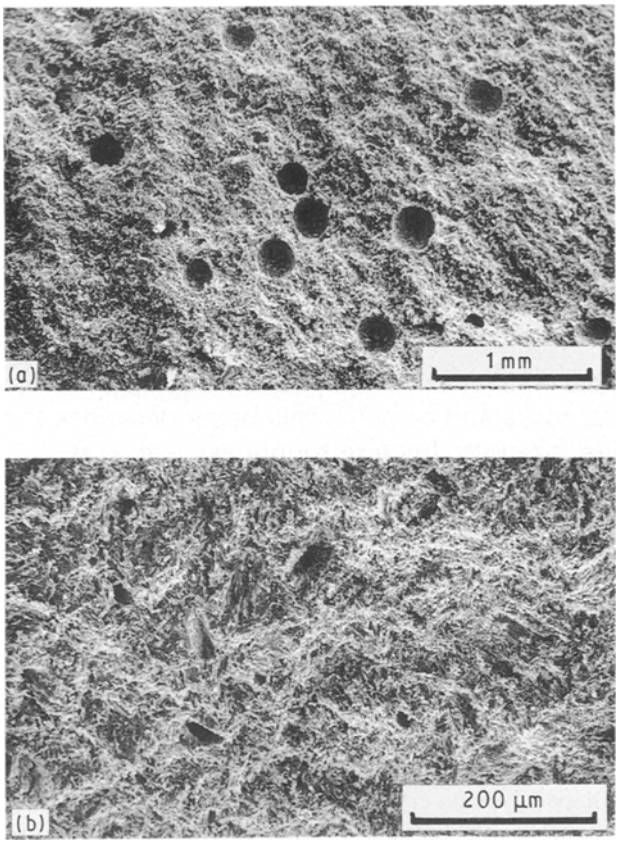

Figure 1 The structure of the plaster: (a) 50% relative density and (b) 70% relative density specimens.

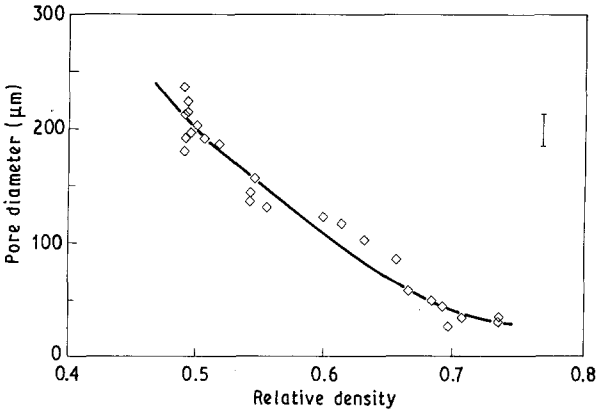

Figure 2 Macropore diameter as a function of relative density of hydrated plaster of Paris.

modulus (by four-point bending, E_{bend}, and under uniaxial compression, E_{comp}), the modulus of rupture under three- and four-point bending (MOR_3 and MOR_4), the fracture toughness, K_{Ic}, by four-point straight-edge-notched beam (SENB), the uniaxial tensile strength, σ_t, and the uniaxial compressive strength, σ_c. In addition, the compressive strengths under biaxial and hydrostatic conditions were also measured. The results for the as-cast material are summarized in Table I, which also lists data from earlier published studies.

Young's modulus, E, was determined from the loading curves in bending and uniaxial compression, as described below.

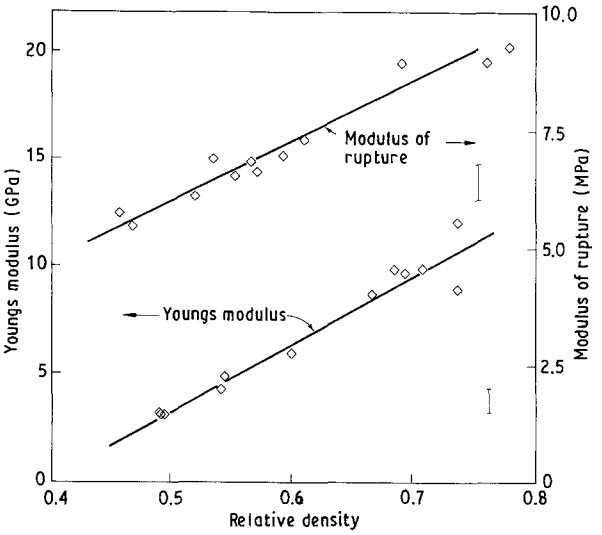

Figure 3 Young's modulus in uniaxial compression and modulus of rupture in four-point bending as a function of relative density.

Four-point bend tests were used to measure the modulus of rupture (Table I). The beam specimens (10 mm × 10 mm × 90 mm) were lightly ground using 1000 grade SiC paper prior to testing in order to remove an outer skin which has a different morphology from the bulk of the specimens. Modulus of rupture values were calculated using the well-known equation

$$MOR_4 = \frac{P\Delta sd}{8I} \quad (2)$$

where P is the fracture load (N), Δs is the difference between major and minor spans, I is the second moment of area of specimen ($bd^3/12$, where b is the width of specimen), and d is the height of specimen. All the specimens displayed purely elastic behaviour up to fast fracture. The variation of modulus and MOR_4 with relative density and associated pore size is shown in Fig. 3. Young's modulus for four-point bending (Table I) was calculated using the elastic beam theory as

$$E_{bend} = \frac{dP}{dx}\frac{\Delta s^3}{4bd^3} \quad (3)$$

The fracture toughness measurements were carried out on rectangular edge-notch beam specimens with the same dimensions as those used for the bending tests. The fracture toughness, K_{Ic} (Table I), was calculated from the analysis of Strawley and Gross [19]

$$K_{Ic} = \frac{P}{b/d}\frac{\Delta s}{d}\frac{3\tau\alpha^{1/2}}{2(1-a)^{3/2}} \quad (4)$$

where τ is a numerical constant, of order unity, which depends on the ratio of notch depth, a, to specimen height, d. The variation of K_{Ic} with relative density and associated pore size is shown in Fig. 4.

Tensile tests proved difficult: the problem is that of achieving alignment. Special rubberized split grips were designed which provided effective gripping of the cylindrical specimens without high hoop stresses [16]. Only results of specimens that fractured within the

TABLE I Properties of plaster of Paris (as cast, 62.5% water)

		Present study	Previous work [17, 18]
Physical properties	Theoretical density ($kg\,m^{-3}$)	2350	–
	Density ($kg\,m^{-3}$)	1170 ± 30	1060
	Total porosity content (%)	51 ± 2	~ 50
	Mean diameter of spherical macropores (μm)	212 ± 18	–
	Mean grain size (μm)	3×15	–
Mechanical properties	Young's modulus (bending) (GPa)	4.5 ± 0.1	–
	Young's modulus (uniaxial compression) (GPa)	4.6 ± 0.3	–
	Modulus of rupture (four-point bending) (MPa)	5.8 ± 0.6	–
	Weibull modulus	6.2	–
	Fracture toughness (SENB), ($MPa\,m^{1/2}$)	0.14 ± 0.015	–
	Uniaxial compressive strength (MPa)	14.6 ± 0.9	12.8
	Hydrostatic compressive strength (MPa)	19.2 ± 1.4	–
	Uniaxial tensile strength (MPa)	3.2 ± 0.6	–

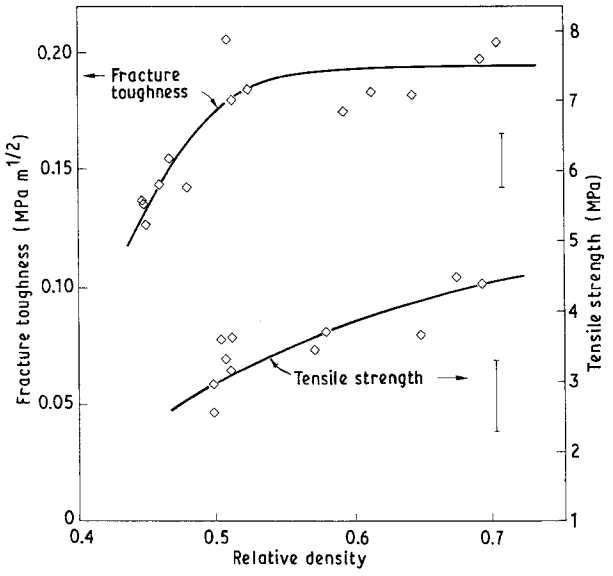

Figure 4 Fracture toughness, K_{Ic}, and the tensile fracture strength as a function of the relative density.

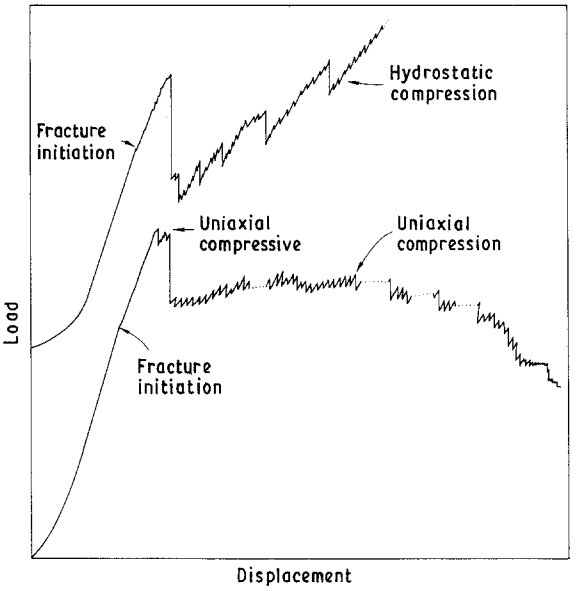

Figure 5 Load–contraction curve for a specimen tested in uniaxial compression (lower curve) and in hydrostatic compression (upper curve).

gauge length were accepted. The tensile strength of the as-cast material is given in Table I. The variation of σ_t with relative density and associated pore size is also shown in Fig. 4.

Compression specimens were prepared by grinding the ends parallel to better than $5\,\mu m\,cm^{-1}$ and perpendicular with respect to the sides to better than 0.2°. To avoid damage to the ends of the specimen and reduce friction between anvils and specimen surface, paper shims were used in all tests. A typical compression curve is shown in Fig. 5 (lower curve). The initiation stress for compressive fracture and the ultimate compression strength are shown in Fig. 6 (lower pair of curves).

Equi-biaxial experiments were carried out both in an Instron and in the SEM compression rig, using wedge grips [16]. Hydrostatic tests were carried out on short cylinders (10 mm diameter × 10 mm height) enclosed in a latex rubber sheath and pressurized in distilled water in a PTFE capsule in a high-pressure vessel (Fig. 7); the arrangement can be used up to

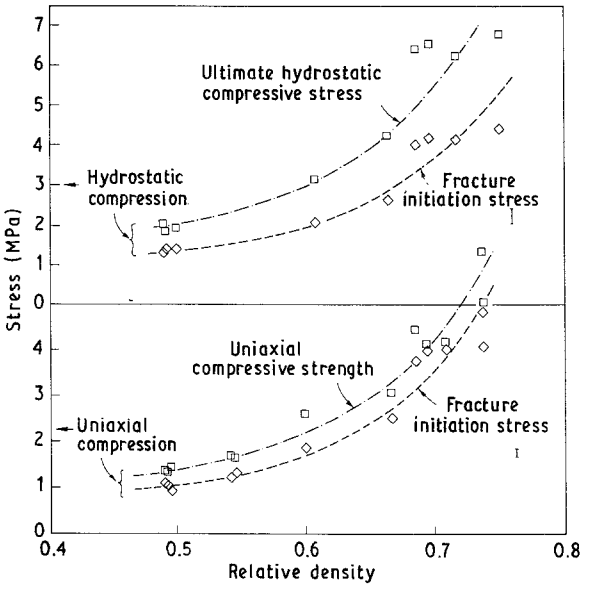

Figure 6 Fracture initiation stress (first non-linearity of the stress–strain curve) and ultimate strength, as a function of relative density, for uniaxial compression (lower curves) and for hydrostatic compression (upper curves).

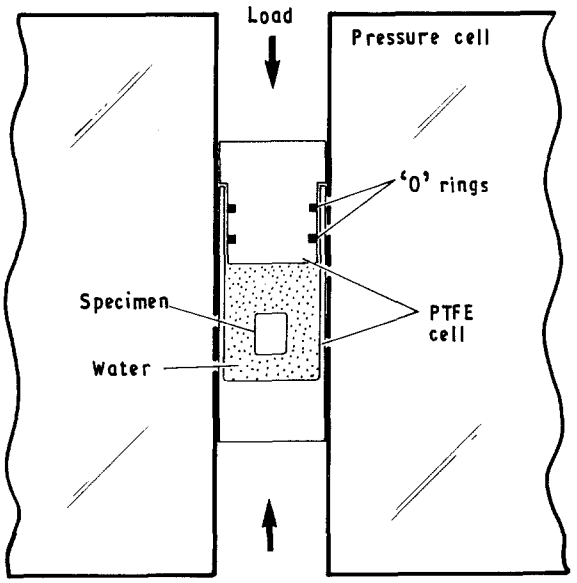

Figure 7 The PTFE cell used in the hydrostatic compression experiments.

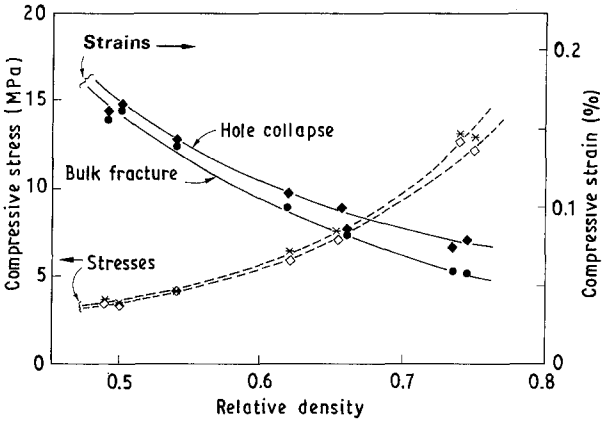

Figure 8 Fracture initiation and hole collapse initiation stress and strain as a function of relative density.

pressures of 1 GPa. All the specimens displayed an elastic response up to the point at which fracture initiated, detected by small steps in the loading curve. A typical pressure–volume curve is shown schematically in Fig. 5 (upper curve). The hydrostatic collapse pressure is plotted against density in Fig. 6 (upper curves). Specimens removed from the cell after testing had been compacted to about three-quarters of their original volume, and were very weak, crumbling easily to a coarse powder.

Specimens were removed from the pressure vessel after various pressures to examine the progressive collapse of the contained porosity. Damage starts at the surfaces of the pores. Collapse proceeds by fracturing of large segments immediately adjacent to the pores which fall inwards, filling the pore. The final stages of collapse are characterized by a general change of pore shape, with general crushing of the surrounding material combined with large-scale fracturing. It appears that pore collapse takes place prior to any bulk fracturing of the material and proceeds extensively before large-scale fracture of specimens.

3.2. Specimens containing cylindrical holes

Uniaxial and biaxial tests were carried out on cubes (approximate size 4.5 mm × 4.5 mm × 4.5 mm) of fully cured plaster of Paris with various densities. A single cylindrical hole of diameter 0.5 mm was introduced by drilling at low speed. The specimens were prepared and tested as before, under uniaxial and biaxial stress states. The observations of pore collapse were made using an *in situ* SEM compression rig.

The stress for initiation of hole collapse and that for bulk fracture initiation in simple compression were measured for a range of densities. The results are summarized in Fig. 8. The sequence of events taking place during uniaxial compressive failure of a cubic specimen containing a drilled hole is illustrated in the micrographs of Fig. 9. The compression direction is vertical. Some bulk fracture of the specimen precedes hole collapse in simple compression. The hole then collapses by the fracture of arc-shaped segments around the walls of the hole, particularly at areas of highest compressive stress concentration at the equator of the hole. The collapse and fracture process is discontinuous. The load needed to continue the collapse process decreases with increasing strain (as in Fig. 5), although the overall specimen collapse is stable up to large strains.

Even a small degree of lateral constraint (i.e. biaxial load) results in the simultaneous initiation of bulk fracture and hole collapse. When the degree of constraint approached equi-biaxial loading, hole collapse preceded the initiation of bulk fracture (Fig. 10). As before, the collapse of the hole involves the inward fracturing of arc-shaped segments from the walls. The collapsed areas become more uniformly distributed around the wall of the hole as an equibiaxial stress state is approached. Hole collapse reaches an advanced state before significant overall specimen collapse. The collapse process is discontinuous, but significantly more stable than in the uniaxial case, i.e. the load required to sustain the collapse process remained constant or decreased very slowly with increasing strain (as in Fig. 5).

4. Discussion

Models for the compressive cracking of brittle solids [2, 14, 15] suppose that cracks initiate at flaws (the flaws might be spherical pores or sharp cracks). The models lead to an expression for the stresses for crack initiation; it is a relationship between the axial stress, σ_1, and the radial stress, $\sigma_3 = \sigma_2$, $(\sigma_1 > \sigma_3)$, which can be written as

$$\sigma_1 = c_1\sigma_3 - c_0 \quad (5)$$

where the constants c_1 and c_0 depend on the nature of the flaws. When cracks nucleate from spherical holes, the constant c_1 is predicted to be about 3.1–3.4 [15]. When, instead, they nucleate from cracks [2, 14] it depends on the coefficient of friction, μ, between the sliding crack faces and ranges from 1–3.5 as μ ranges from 0–0.7. (Experimental results on crack initiation in Westerly granite, quoted in [20], suggest a value of

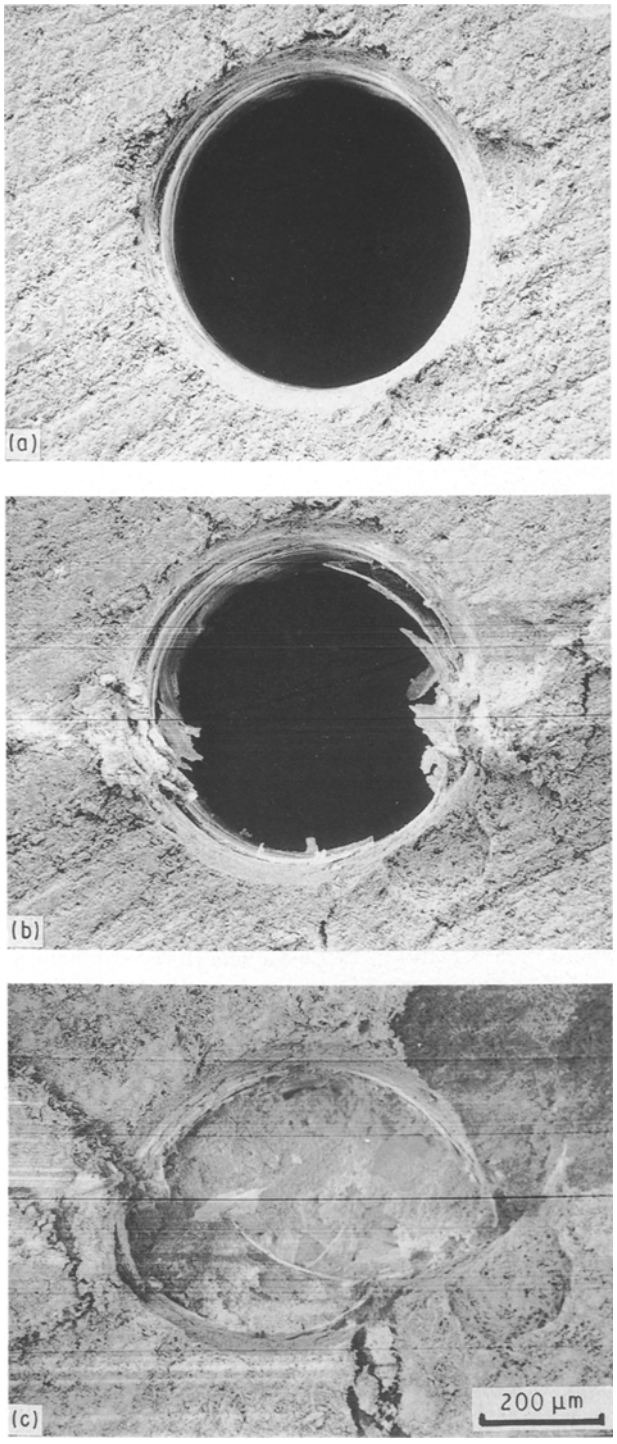

Figure 9 Progressive failure of $CaSO_4$ with a hole under uniaxial compression.

c_1 of approximately 2.8 for both pores and cracks for this material.) The constant c_0 depends on the fracture toughness, K_{Ic}, and the flaw size, $2a$. For pores, $c_0 \simeq 1.6K_{Ic}/(\pi a L_0)^{1/2}$, where $2a$ is the diameter of the pore divided by the pore radius). For sharp cracks, $c_0 = 3.1\ K_{Ic}/(\pi a)^{1/2}$, where $2a$ is the length of the inclined crack. Both the form of Equation 5 and the $c_0 = 3.1K_{Ic}/(\pi a)^{1/2}$, where $2a$ is the length of the inclined crack. Both the form of equation 5 and the constants are almost identical for both extreme types of flaw; it may therefore be considered as a general criterion for damage initiation in compression [21]. Final fracture involves crack–crack interaction. It is treated in earlier publications [14, 15, 21].

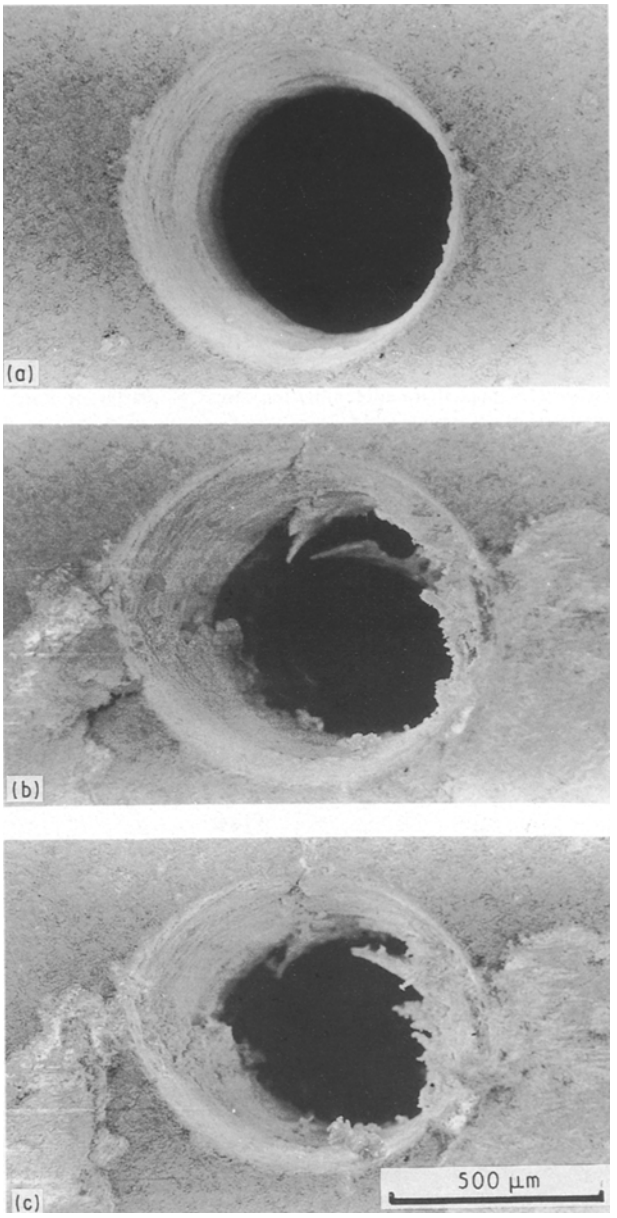

Figure 10 Progressive failure of $CaSO_4$ with a hole under constrained uniaxial compression; $\sigma_2/\sigma_1 \approx 0.2$.

For uniaxial compression $\sigma_3 = 0$ and Equation 5 simplifies to

$$\sigma_1 = -1.6K_{Ic}/(\pi a_p L_0)^{1/2} \text{ (holes)} \qquad (6a)$$

or

$$\sigma_1 = -3.1K_{Ic}/(\pi a_c)^{1/2} \text{ (cracks)} \qquad (6b)$$

where a_p and a_c are the dimensions of the pores and cracks, respectively. A plot of uniaxial fracture initiation stress (as determined by the first non-linearity of the load–displacement curve) versus $K_{Ic}/(\pi a)^{1/2}$ should be linear through the origin and yield a "best-fit" value for L_0. The plot (Fig. 11) shows that the fracture initiation model fits the observations well with a calculated (best-fit) value for $L_0 \simeq 1.5$.

When hydrostatic stress is applied to a porous body, shear stresses appear at and near the pores (Fig. 12). The local stress state can be described by a radial stress, σ_r, and two equal tangential stresses,

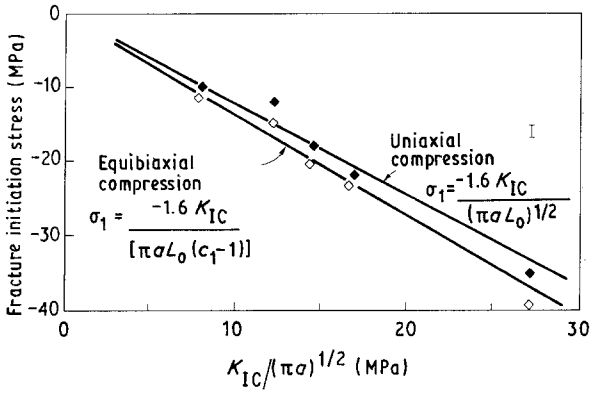

Figure 11 Uniaxial fracture initiation stress of plaster of Paris: comparison with models [15, 21].

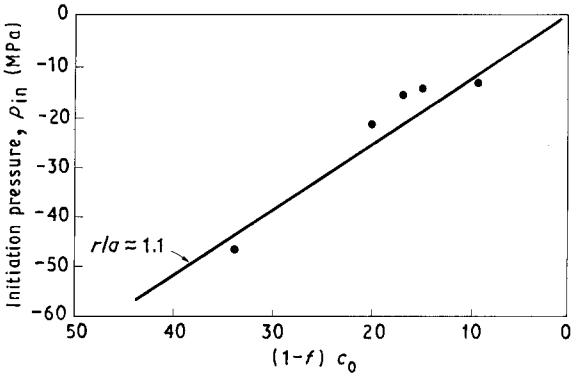

Figure 13 The hydrostatic stress for fracture initiation plotted against $(1-f)c_0$, following Equation 11. The line corresponds to an initiation depth $r/a = 1.1$.

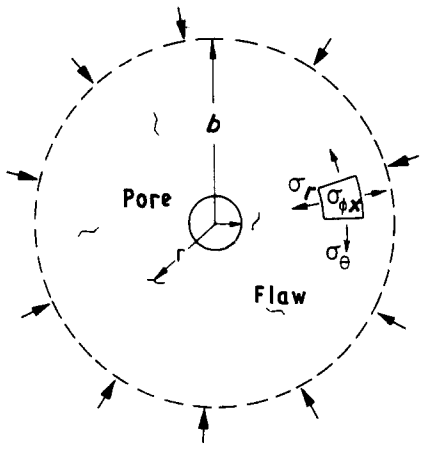

(a)

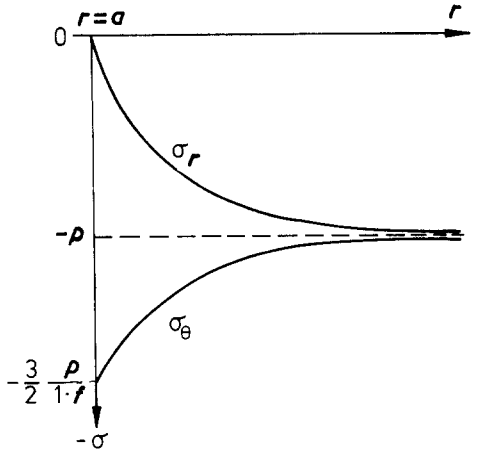

(b)

Figure 12 (a) Stresses around a spherical pore subjected to hydrostatic pressure, p, and (b) their variation with distance from a pore, r (Equations 7 and 8).

σ_θ, where [22]

$$\sigma_r = -p\frac{b^3}{r^3}\frac{(r^3-a^3)}{(b^3-a^3)} \tag{7}$$

$$\sigma_\theta = \sigma_\varphi = -p\frac{b^3}{2r^3}\frac{(a^3+2r^3)}{(b^3-a^3)} \tag{8}$$

Far from the pore all stress components approach the hydrostatic stress level, $-p$, but, whereas the radial component, σ_r, decreases from 0 at the pore surface to $\simeq -p$ at $r = b$, the tangential components increase from a minimum value $= -3/2p/(1-f)$ (where $f = a^3/b^3$ is the volume fraction of pores in the material) at the pore surface, to the value $-p$ at $r = b$, as shown in Fig. 12.

Applying the fracture nucleation Equation 5 to the case of hydrostatic compression of porous brittle materials, we find (because σ_r is less compressive than σ_θ)

$$\sigma_\theta = c_1\sigma_r - c_0 \tag{9}$$

where $c_1 \simeq 3.1$ and $c_0 \simeq 1.6K_{Ic}/(\pi a_p L_0)^{1/2}$ as before for holes. Substituting for σ_r and σ_θ we obtain

$$-p_{in}\frac{b^3}{2r^3}\frac{(a^3+2r^3)}{(b^3-a^3)} + c_1 p_{in}\frac{b^3}{r^3}\frac{(r^3-a^3)}{(b^3-a^3)} = -c_0 \tag{10}$$

using $f = a^3/b^3$ and solving for p_{in} (the hydrostatic stress for fracture initiation) we finally find

$$p_{in} = \frac{2r^3/a^3(1-f)c_0}{1+2c_1-2(c_1-1)r^3/a^3} \tag{11}$$

The equation shows that fracture initiation is easiest at the surface of the hole ($r = a$), and becomes rapidly more difficult as r increases. The initiation pressure, p_{in}, becomes infinite at $r/a = [(1+2c_1)/(2c_1-2)]^{1/3}$ ($\simeq 1.2$ for $c_1 \simeq 3.1$), beyond which point no fracture would be expected to initiate.

In order to compare the hydrostatic compression model introduced above (Equation 10) with the results obtained in this work the hydrostatic fracture initiation stress, p_{in}, has been plotted versus $(1-f)K_{Ic}$ in Fig. 13. It is clear that the results can be described quite well by a linear relation through the origin as suggested by the model. From this graph the "best-fit" value of r/a is $\simeq 1.1$ which lies within the "critical" r/a value predicted by the model and with the value of L_0 found for the uniaxial compression case above. Thus fracture initiation in this material occurs very close to the pore surface as predicted by the model.

Finally, the overall behaviour of the plaster of Paris is summarized by the surfaces of Fig. 14, which show the combination of stresses required to cause crack

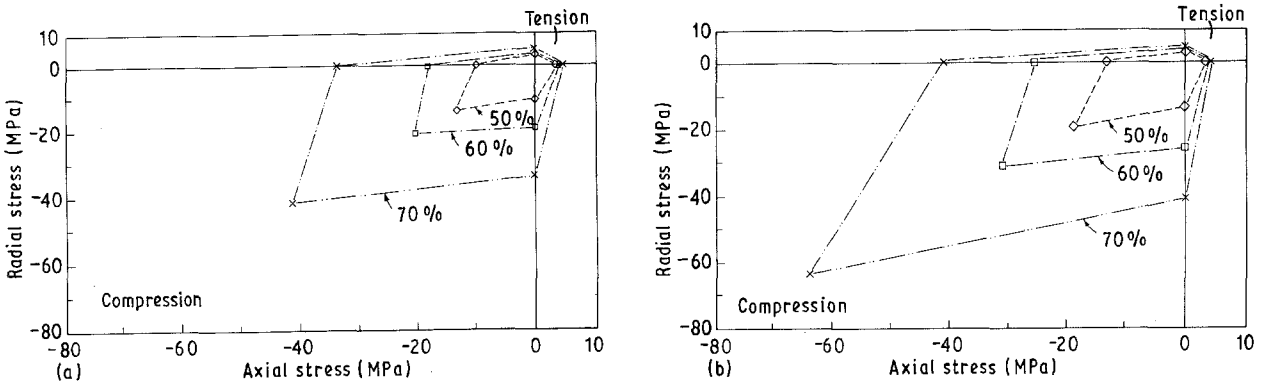

Figure 14 (a) Fracture initiation, and (b) final collapse surfaces for plaster of Paris, for three relative densities.

initiation, at (a), and final failure, at (b), for three relative densities.

5. Conclusion

Plaster of Paris can be used as a model material to study fracture phenomena in brittle porous solids. To do this, the properties of the plaster are needed: they are determined and listed in this paper. The material is then used to study spalling at holes, in multiaxial stress states. The ease of fabrication and manipulation make plaster an attractive model material for such studies.

Acknowledgements

We thank the technical staff of the Materials Group, Richard Brand, Brian Butler, Alan Heaver, Simon Marshall and Oscar Skulskyj, who provided invaluable technical support. The research was made possible through the financial support of the United States Air Force Office of Scientific Research under grant number AFOSR-87-0307.

References

1. A. A. GRIFFITHS, in "Proceedings of the 1st International Congress on Applied Mechanics", Delft (Delft University Press, 1924) p. 55.
2. S. NEMAT-NASSER and H. HORII, *J. Geophys. Res.* **87** (1982) 6805.
3. D. GRIGGS and H. HANDIN, (eds), "Rock Deformation", (Geological Society of America, Waverl Press, Baltimore, 1960) Ch. 13.
4. *Idem, Geol. Soc. Amer. Mem.* **79** (1960) 347.
5. F. A. McCLINTOCK and J. B. WALSH, in "Proceedings of the 4th US Congress on Applied Mechanics" (ASTM, Interscience, 1962) p. 1015.
6. S. A. F. MURRELL, in "Rock Mechanics", edited by C. Fairhurst, Proceedings of the 5th Symposium on Rock Mechanics (Pergamon Press, Oxford, 1963) p. 563.
7. *Idem, Geophys. J. R. Astron. Soc.* **10** (1965) 231.
8. S. A. F. MURRELL and P. J. DIGBY, *ibid.* **19** (1970) 309.
9. *Idem, ibid.* **19** (1970) 499.
10. J. C. JAEGER and N. G. W. COOK, "Fundamentals of Rock Mechanics" (Methuen, London, 1969).
11. S. KOBAYASHI, *J. Soc. Mater. Sci. Jpn* **20** (1971) 164.
12. J. B. NEWMAN, in "Developments In Concrete Technology-I", edited by F. D. Lydon (Applied Science, 1979).
13. *Idem, Appl. Sci.* **5** (1978) 151.
14. M. F. ASHBY and S. D. HALLAM, *Acta Metall.* **34** (1986) 497.
15. C. G. SAMMIS and M. F. ASHBY, *ibid.* **34** (1986) 511.
16. G. VEKINIS, M. F. ASHBY and P. W. R. BEAUMONT, Cambridge University Engineering Department Reports CUED/C-MATS/TR 148 (1989), CUED/C-MATS/TR 174 (March 1990).
17. A. DINSDALE, "Pottery Science: Materials, processes and products", (Horwood, London, 1986).
18. F. SINGER and S. S. SINGER, "Industrial Ceramics" (Chapman and Hall, London, 1962).
19. J. E. STRAWLEY and B. GROSS, in "Cracks and Fracture", American Society for Testing and Materials Special Technical Publication 601 (ASTM, Philadelphia, PA, 1976) pp. 559–79.
20. M. L. KACHANOV, *Mech. Mater.* **1** (1982) 19.
21. M. F. ASHBY and C. G. SAMMIS, *PAGEOPH* **133** (1990) 481.
22. R. J. ROARK and W. C. YOUNG, "Formulas for stress and strain", 5th Edn (McGraw-Hill, New York, 1975).

Received 7 January
and accepted 4 February 1992